A Limit to Accelerated Free-Sintering: Nano-Phase Separation Interferes With Organic Debinding

YANNICK NAUNHEIM, ALICE PERRIN, CHRISTIAN E. OLIVER,
KATHERINE STONE, and CHRISTOPHER A. SCHUH

Nano-phase separating Ni–12 at. pct Ag powders are processed *via* high-energy ball milling and brought into a supersaturated state with a reduction of the grain size to the nanocrystalline scale, a combination that is designed to encourage rapid densification by phase separation upon heating. This unstable powder is then characterized by dilatometry, *in-situ* x-ray diffraction, thermogravimetry and microstructure analysis for sintering cycles up to 940 °C. However, these powder compacts exhibit excessive pore evolution and significant macroscopic swelling caused by removal of the organic process additives. This competition of organic removal with densification is known in nanocrystalline metals, but the present study adds an additional dimension of phase separation, which shifts the dominant swelling mechanism as the formation of the second phase traps the volatilizing organics and hinders the debinding process. The creep swelling and overall loss in relative density is then dominated by the creep deformation of the second Ag phase. The interference between organic removal and low-temperature onset of consolidation represents a new challenge to efforts aimed at rapid free sintering and should guide the design of rapidly sintering alloys; specifically, the present work emphasizes the need to select alloys that have their sintering-accelerating phase separation temperature above the range where gases are evolved.

I. INTRODUCTION

WHILE there are many additive manufacturing technologies based on layer-by-layer build-up from metal powders, the prominence of different underlying strategies for powder consolidation is in rapid flux as the field develops.[1–3] In particular, recent commercial activities in green body printing and sintering methods[4] foreshadow a need for more studies on free sintering methods and the achievement of full density from printed green bodies. The relatively lower green densities achievable especially by methods such as bound metal deposition[5] and binder jet-printing[6,7] require renewed focus on methods that can achieve a higher degree of densification and faster mass transport than might be typical for press-and-sinter powder metallurgy operations. For these reasons, as well as the general improvement of productivity and conservation of energy, studies exploring strategies for accelerated sintering are expected to be of special interest in the context of metal additive manufacturing over the coming decades.

There are various strategies applied to expedite the degree of sintering in metal powders through an increased rate of mass transport, which are accompanied by diverse merits and demerits. The most prominent of these methods in the powder metallurgy literature is partial melting, typically referred to as liquid phase sintering. In the context of 3D printing, liquid phase sintering has a double-edged character as it accelerates diffusion in the liquid phase and promotes rapid consolidation, but by definition involves melting and a reduced strength that permits the rearrangement of the powder particles.[8–10] The resulting high deformation rate or gravitational slumping is a major concern for printed green bodies, which are intended to maintain their net shape after sintering.[11,12] Besides these effects of creep, other deficiencies of liquid phase sintering include the build-up of residual stress,[13,14] void generation[15,16] and microstructural evolution.[17–19]

Another common method of accelerated sintering, solid-state activated sintering, has similar properties to liquid phase sintering but occurs entirely in the solid

YANNICK NAUNHEIM, CHRISTIAN E. OLIVER, KATHERINE STONE, and CHRISTOPHER A. SCHUH are with the Department of Materials Science and Engineering, Massachusetts Institute of Technology, 77 Massachusetts Avenue, Cambridge, MA 02139. Contact e-mail: schuh@mit.edu ALICE PERRIN is with the Department of Materials Science and Engineering, Massachusetts Institute of Technology and also with the Materials Science and Technology Division, Oak Ridge National Laboratory, Oak Ridge, TN.

state. For this approach, alloying of refractory metals—typically with transition metals, such as Pd, Pt, Ni and Fe—enhances the diffusion kinetics.[20–22] Mechanistic discussions of this phenomenon are varied,[23] but it has been observed that the apparent grain boundary diffusion rate is increased, as compared to the unalloyed state[24–26]. Employment of this concept enabled binder jetting of tungsten and tungsten carbide in the work of Stowovy et al.[27] and Enneti et al.,[28,29] respectively, at the expense of a coarsened final microstructure. However, both strategies address the challenge to enhance the atomic transport, which makes them potential candidates for free-standing sintering techniques.

A third sintering acceleration strategy is based on the use of systems that phase separate, and inducing nanoscale structures that kinetically encourage phase separation at low temperatures.[30,31] Termed 'nano-phase separation sintering', the process begins with a powder alloy driven far from thermodynamic equilibrium, which can be reached through e.g., high-energy milling. Solute atoms are thereby incorporated into the solvent lattice in a concentration far beyond the solubility limit. Accelerated mass transport is achieved by providing many rapid diffusion pathways through a refinement of the grain size, also a natural result of milling.[30,32] Upon heating (as during a sintering cycle), the excess solute is ejected from solution and can decorate the particle surfaces, arriving there by diffusing out of solution along the numerous grain boundaries. During nano-phase separation sintering, the exploitation of both the supersaturated powder and provision of numerous rapid diffusion pathways accelerates consolidation at low temperatures, while also preventing excessive grain growth and generally retaining finer grains. The method can produce microstructures that are refined by more than one order of magnitude compared to liquid phase[33–35] and activated solid-state sintering,[36,37] and it is a free sintering technique, which makes it a suitable candidate for bulk green body printing. The method has been successfully used for at least two alloys (W–Cr[5,30] and Cr–Ni[32,38]) with bound metal deposition 3D printed parts.

Whatever the sintering method, pressure-less powder printing techniques, such as binder jetting and bound metal deposition, require the addition of organic matter to facilitate initial binding of the powders in the shape of the green body. These additives are subsequently removed before sintering, sometimes through chemical means, but almost always with a thermal decomposition final step. Such organics decompose into gaseous products that are lost readily at low or intermediate process temperatures,[39–41] typically prior to the onset of powder consolidation. Although the thermal decomposition temperature of organic binders[7] is reported to be between 240 °C to 380 °C[42] and 200 °C to 500 °C,[43] debinding temperatures (from a green body) are a bit higher in practice. For instance, Nandwana et al.[44] performed binder jet-based 3D printing of Inconel 718 powder and employed a step-wise temperature profile with the dissolution of the organic binder completed at ~ 700 °C; this is still well below the temperature range where consolidation was reported (1000 °C to 1300 °C). Similarly, Mostafaei et al.[45] used binder jetting on Inconel 625 with removal of the binder up to 1000 °C and sintering between 1225 °C and 1300 °C. Inconel 718 powder was injection molded by Hnatkova et al.[46] with step-wise treatment at 440 °C for thermal dissolution of the organic binder and well distinguishable sintering kinetics at 1270 °C.

The need for such organic removal poses an interesting challenge to accelerated free sintering, which has received little attention in the literature to date. In our recent work we highlighted the importance of the competition between organic removal and sintering densification specifically in single-phase nanocrystalline metals.[47] There we showed that accelerated densification associated with nanocrystalline grains could exacerbate this competition and lead to gas entrapment and swelling. However, that concept is more broadly applicable to all forms of sintering acceleration, and thus a major purpose of the present paper is to further illustrate this issue in a system designed for nano-phase separation at low temperatures, Ni–Ag. Such low-temperature phase separation is associated with rapid densification in some metals, as noted above, but in the Ni–Ag system it leads to gas entrapment. What is more, this system is found to provide further independent validation of a mechanistic inference made in our prior work,[47] namely, that at intermediate temperatures the gas-pressure-induced swelling is kinetically rate-limited by creep deformation.

II. MECHANICAL ALLOYING OF NICKEL–SILVER

This work explores the Ni–Ag system because of its prominent tendency for phase separation even far beyond the solid state.[48–50] The broad miscibility gap in the solid-state and the lower melting point of Ag align well with two key requirements for nano-phase separation sintering, namely the tendency for phase decomposition at low-temperature, and to form interparticle necks readily.[32] Thus, upon heating of a supersaturated nanocrystalline powder, we expect this system to rapidly evolve a two-phase structure in which Ag bridges hold together the Ni powders. This two-phase structure is expected to persist thereafter, because there is no solubility at any temperature, so the alloy is specifically relevant to explore structure evolution in a two-phase system; as we shall see this leads to a clean test of the dominant swelling mechanism for systems with entrapped gas.

To design an alloy composition with maximum solute supersaturation and phase separation tendency, as for other immiscible binary systems[51,52] a difference in their mechanical strengths[53,54] has been suggested as a guideline to predict the limit of mechanical mixing at the atomic scale. Cordero and Schuh[55] provided a quantitative framework for this phenomenon based on the difference in strength of each component when having a nanocrystalline grain size (as is a typical result during milling). They evaluated the normalized strength differential[55]

$$\Delta = \frac{\left| \sigma_{y,\mathrm{Ni}} - \sigma_{y,\mathrm{Ag}} \right|}{\frac{\sigma_{y,\mathrm{Ni}} + \sigma_{y,\mathrm{Ag}}}{2}}, \qquad [1]$$

where the yield strengths σ_y of the constituent phases are evaluated at a grain size of ~ 10 nm as typically result upon milling. Using available data for the Hall–Petch constants[56] gives values of $\sigma_{y,\mathrm{Ni}} = 2380$ and $\sigma_{y,\mathrm{Ag}} = 1050$ MPa, yielding a value of ~ 0.77 for the strength differential parameter Δ. According to the evaluation by Cordero and Schuh,[55] this is a high value for the strength differential and is expected to speak to a substantially limited solubility of the driven system. Using kinetic Monte Carlo simulations at a nearby value of $\Delta = 0.7$, they reported a maximum solubility of ~ 10 to 12 at. pct at half of the homologous temperature.

Following this guideline, we thus work with 12 at. pct Ag powder (Inframat Advanced Materials, 99.95 pct, 1.2 to 2.0 μm) to be mechanically alloyed into Ni powder (Alfa Aesar, 99.9 pct purity, 3 to 7 μm particle size) on a SPEX 8000D Mixer/Mill with a ball-to-powder ratio of 10:1 in a glovebox maintained under an ultra-high purity Ar atmosphere. Fracturing and cold-welding of the powder during milling is controlled using 5 wt pct Ethanol (C_2H_6O) as process control agent (PCA). The chemical composition is determined using wavelength-dispersive X-ray diffraction (JEOL JXA-8200; 15 kV accelerating voltage, 10 nA beam current, spot size ~ 1 μm^2) on at least 4 powders and is shown in Table I. The pickup of (trace) contamination is due to the wear of the grinding media during milling and reflects typical constituents of hardened steel. The powder is ball-milled for 2, 5, 10 and 20 hours to track the chemical mixing between Ni and Ag and structural evolution during high-energy ball milling. Milling for longer than 20 hours is avoided, as it typically leads to an increased contamination in the powders.[55] The microstructures are imaged using a Merlin Zeiss high-resolution scanning electron microscope (HR-SEM) in backscatter mode (BSD) at a working distance of about 10 mm, a voltage of 15 kV and a current of 2 pA. The Ni–Ag powder is characterized through XRD on a Panalytical X'Pert PRO using Cu-K$_\alpha$ radiation with a wavelength $\lambda = 1.5418$ Å and a step size of 0.0167 deg, operated at 45 kV and 40 mA for voltage and current, respectively. The micrographs for different milling times in Figures 1(a) through (d) suggest a refinement of the morphology and a reduction of the phase contrast as the lamellae thickness decreases. Since chemical homogenization is the product of shearing across the interphase boundaries, a refined lamellae structure speaks to structural and chemical evolution of the phases inside the powders. The diffraction patterns (e) for all interrupted ball milling runs and the reference patterns for Ni and Ag confirm the evolution of chemical mixing by the broadening and flattening of the characteristic Ag peaks.

The mean spacing λ between Ag-rich phase regions inside the powder particles is determined by

$$\lambda = \frac{1 - V_{\mathrm{Ag}}}{N_{\mathrm{L}},} \qquad [2]$$

where V_{Ag} is the volume fraction of Ag ($V_{\mathrm{Ag}} = 0.18$ for 12 at. pct Ag) and N_{L} is the number of intercepts of Ag per unit length line.[57] The evolution of the lattice parameter for each phase is assessed by Rietveld refinement. The average grain size is determined from the peak broadening corrected by the lattice strain using a classical Williamson–Hall analysis[58] and instrumental contributions using a NIST LaB$_6$ reference. The quantitative decrease of the Ag-rich phase mean spacing λ in Figure 1(f) maps to atomic-level mixing, which can also be assessed by a shift of the lattice parameter.[59] The results in Figures 1(g) and (h) illustrate how the Ni lattice expands through the incorporation of larger Ag atoms and vice versa, as mixing progresses. Employing Vegard's law[60] yields an atomic enrichment of 12.3 and 9.8 at. pct for Ag in Ni and Ni in Ag, respectively, after milling for 20 hours; this is nearly complete mixing given the global composition of 12 at. pct Ag in the system (for as-milled powder, see Supplementary Fig. S1). However, it is not literally complete mixing, as there are clearly discernible reflections (and grain size measurements) for both Ni and Ag phases throughout milling. This agrees with the changes of the volume fraction of the Ag phase upon high-energy ball milling. To a first order estimate, a change in the integrated intensity (area) of a phase peak speaks directly to a change in volume fraction during mechanical alloying.[52] The ratio of the integrated intensities of the characteristic Ag peak at a later stage of the milling process I referenced to an initial value I_0, as for an unmilled reference pattern for Ag (cf. Figure 1(e)), is another indicator for the partial chemical homogenization. The volume fraction gradually decreases and a fraction of ~ 0.13 (Figure 1(i)) is obtained for mechanical alloying after 20 hours, suggesting some degree of incomplete mixing.

Mechanical alloying of the Ni–Ag couple has been subject of several prior studies[61,62] and solubilities of

Table I. Chemical Composition of the Powder After 20 h of High-Energy Ball Milling Determined by Wavelength-Dispersion Spectroscopy

Element	Ni	Ag	Fe	Cr	Mn	Si
At. Pct	0.8736 ($\pm$ 0.088)	0.1202 ($\pm$ 0.0479)	0.0058 ($\pm$ 0.014)	0.0001 ($\pm$ 0.00016)	0.0002 ($\pm$ 0.00174)	0.00005 ($\pm$ 0.00095)

The contamination of the powder with elements such as Fe, Mn, Cr and Si arises from wear with the grinding media during high-energy ball milling
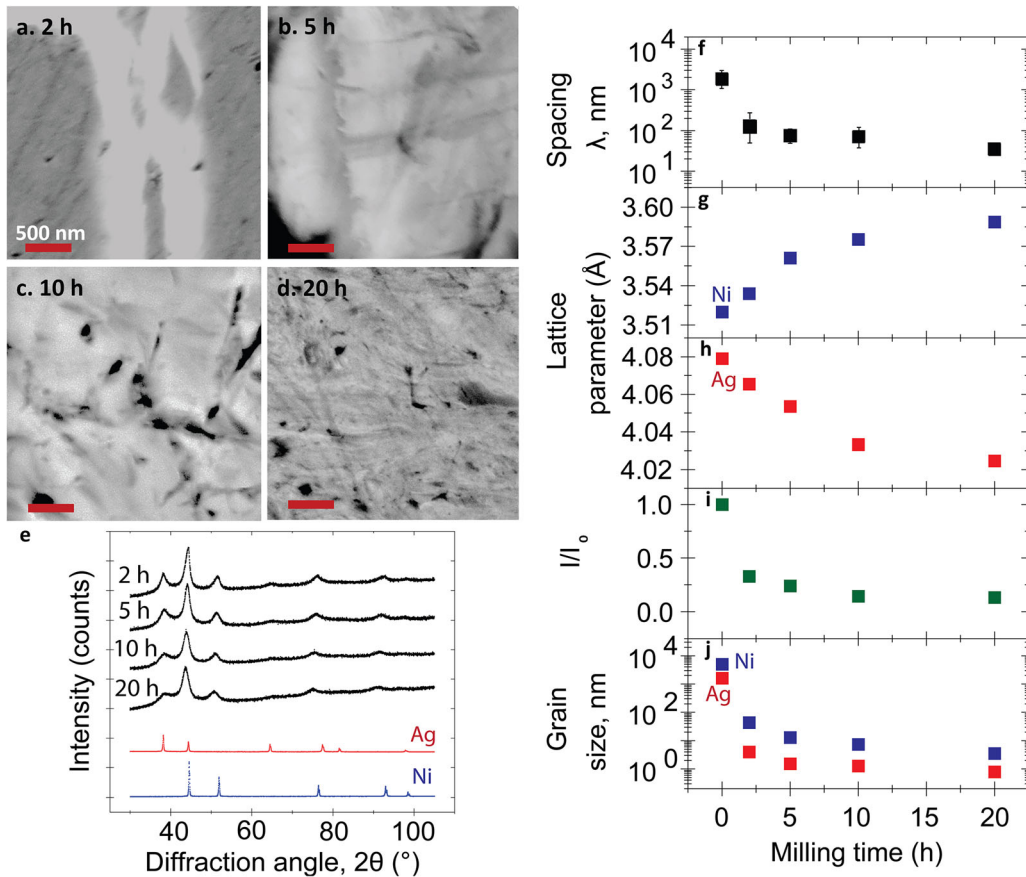
Fig. 1—An overview of the high-energy milling of the Ni–Ag system. Micrographs of the Ni–Ag powder for different ball milling times (*a*) through (*d*). Brighter and darker lamellae are Ag- and Ni-rich phases, respectively. Scale bars are all 500 nm. Milling leads to a refinement of the lamellae and an advancement of the chemical homogenization as reflected in the reduced contrast. (*e*) X-ray diffraction pattern evolution for different milling times and the reference patterns for un-milled Ag and Ni, showing the gradual loss of the Ag peaks. This is confirmed by the evolution of the structure for various milling times (2, 5, 10 and 20 h): (*f*) Mean spacing of the Ag phase as extracted from the micrographs in (a) through (d). (*g, h*) Both phases show an enrichment with unlike atoms as suggested by the expansion of the Ni lattice with larger Ag atoms and the contraction of the Ag lattice with smaller Ni atoms. (*i*) The progress of interphase mixing is also documented by the evolution of the relative integrated intensity of the Ag phase (referenced to the integrated intensity after 2 h of high-energy ball milling). (*j*) Although the grain size of both Ni and Ag phases refine to the smallest grain size scale, Ag refines at a much faster rate initially due to the clear mechanical strength mismatch between both phases.

Ag into Ni up to about 7[54] and 20 at. pct[63] have been reported. This finite mixing capability is in line with the dissolution limit on the border of ~ 12 at. pct in this work, and highlights the significant resistance of Ni–Ag to form a homogeneous solid solution. There are two main reasons why a mechanically alloyed system may not achieve full mixing. The first of these is more relevant to elevated temperatures, where atomic diffusion towards global equilibrium opposes the forced ballistic mixing caused by deformation.[53,64] In the present system we do not expect significant diffusional rearrangements to occur because of the low-temperature of milling (which is not likely over about 200 °C). As we shall see in the next section, phase separation does not kinetically set on in these powders until about 400 °C. Therefore, the second reason for incomplete mechanical alloying may be more likely in this case, i.e., due to mechanical strain localization during milling. This is the mechanism underlying Eq. [1] above used to identify the expected non-equilibrium solubility, and the fact that

the present alloy appears to be right on the edge of full dissolution is in line with that mechanistic explanation.

Additional support for the mechanical mismatch theory of incomplete mixing can be provided by observations of its underlying mechanism: strain localization in the weaker phase.[53] In the present case such evidence is indeed provided by the grain size evolution measurements in Figure 1(j). Although the decrease in grain size follows an exponential refinement trend[65] for both phases, it proceeds faster in Ag than Ni, and Ag is always at a finer grain size; strain localization in the Ag phase may be suggested by this trend. There is additional support from direct visual observation of the microstructures in the early phases of milling, in which the flow of the softer element (Ag) around the harder element (Ni)[66] is seen (Figure 1(a)).

At the end of milling, the powders are mostly chemically homogeneous in a solid Ni–Ag solution at a concentration far out-of-equilibrium. While there is evidence of a small amount of silver-rich Ag–Ni solid

solution, this too is far from equilibrium. The strong tendency for full phase separation of this system has important consequences during subsequent heating, as we explore in what follows.

III. NANO-PHASE SEPARATION

With the Ni powder being supersaturated with Ag atoms and in a thermodynamic state far out-of-equilibrium, we aim to characterize the onset of nano-phase separation upon heating. In the same manner as we recorded the progress of mechanical alloying, we monitor the process of phase separation first through changes in the lattice parameter. We perform *in-situ* XRD on a Panalytical X'Pert with the same radiation wavelength, step size, voltage and current as described above. The ball-milled powders are therefore heated to the measurement range (200 °C to 550 °C) in a protective industrial-purity He atmosphere. One XRD pattern herein is recorded for a scan time of about 20 minutes at each temperature increment of 10 °C, whereas the temperature is adjusted in between each measurement
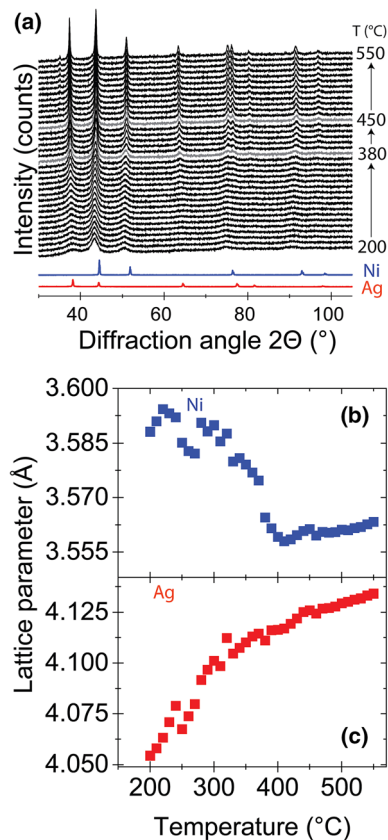
at a heating rate of 60 °C/min, followed by a hold of 5 minutes to allow the system to equilibrate before scanning. For each pattern at a given temperature, lattice parameter (and grain size, cf. Fig. S3) are determined by the procedure as described for the ambient XRD measurements above. Figure 2(a) shows the XRD patterns between 200 °C and 550 °C in comparison with the individual (bulk) reference patterns for Ni (blue) and Ag (red). Up to a temperature of 300 °C, the XRD patterns exhibit the presence of a fine Ni phase, until the characteristic Ag peaks gradually sharpen for further increased temperature. By 450 °C, the dual-phase microstructure is clearly established. This is confirmed by the evolution of the lattice parameter for Ni and Ag in Figures 2(b) and (c), which reveals a declining size of the Ni lattice parameter and an inverse evolution of the Ag phase. The quantitative measurements in Figures 2(b) and (c) also suggest a decomposition process that is complete (at a very slow heating rate on the order of ~ 20 °C/h or ~ 0.3 °C/min on average) by about 400 °C.

The decomposition kinetics of the Ni–Ag powders are also assessed under constant heating rate experiments *via* differential scanning calorimetry (DSC), using a STA 449 F3 Jupiter from Netzsch up to 600 °C at various heating rates (5 °C/min, 10 °C/min, 15 °C/min and 20 °C/min) in a protective Ar atmosphere. For a system with a limited solubility (such as Ni–Ag), we expect the emergence of a clear exothermic heat signal upon phase separation. Indeed, the heat flow signal in Ni–Ag is clearly of exothermic nature over most of the temperature window. It is well-known that ball-milled powders are non-equilibrium structures with a large concentration of excess defects, e.g., vacancies and grain boundaries. Upon heating, however, excess amounts of vacancies[67] annihilate and grain boundaries relax[68] at a typically much lower temperature than the exothermic peak observed in Figure 3.

Fig. 2—(*a*) XRD patterns at temperatures between 200 °C and 550 °C for the high-energy ball-milled Ni–Ag alloy powders and the un-milled reference patterns for Ni (blue) and Ag (red) at room temperature. The emergence of the characteristic Ag peaks is an indicator for the onset of phase separation, and becomes clearer at temperatures beyond 300 °C; the phase separation is also reflected in the evolution of the individual lattice parameters of Ni and Ag as shown in (*b*) and (*c*), respectively, back to the expected values of the pure constituents (Color figure online).
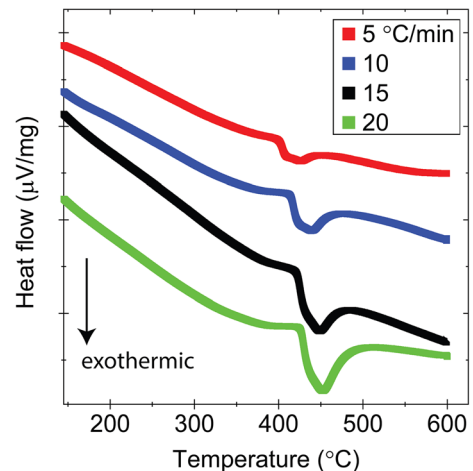

Fig. 3—Differential scanning calorimetry (DSC) curves for Ni–Ag powders heated up to 600 °C at various heating rates. The powders exhibit exothermic behavior with a distinct release of heat at ~400 °C, which corresponds to the onset of phase separation. A more detailed analysis on the heat flow rate and a Kissinger-type kinetic analysis can be found in Figs. S4 and S5, respectively.

The agreement of this exothermic peak temperature with the phase separation seen in the XRD data of Figure 2 instead confirms its source, and further confirmation is provided by direct microstructural and chemical characterization. For that, Ni–Ag powder is annealed isothermally at 450 °C for 4 hours under a protective Ar atmosphere with 4 pct H_2 and the surface of the powders is characterized using SEM in backscatter mode (under the conditions as described before) and by means of energy-dispersive spectroscopy, as shown in Figures 4(a) and (b), respectively. The powder surface is covered by the presence of small particles (Figure 4(a)), which are Ag-rich (b), confirming that the phase decomposition process has already taken place at a temperature of 450 °C. Further, the phase separation leads to preferential decoration of the powder surfaces, exactly as intended to enhance the connectivity and densification of the powder compact. We thus turn our attention to the sintering behavior as we expect the formation of interparticle necks to improve the relative density of the powder compact.
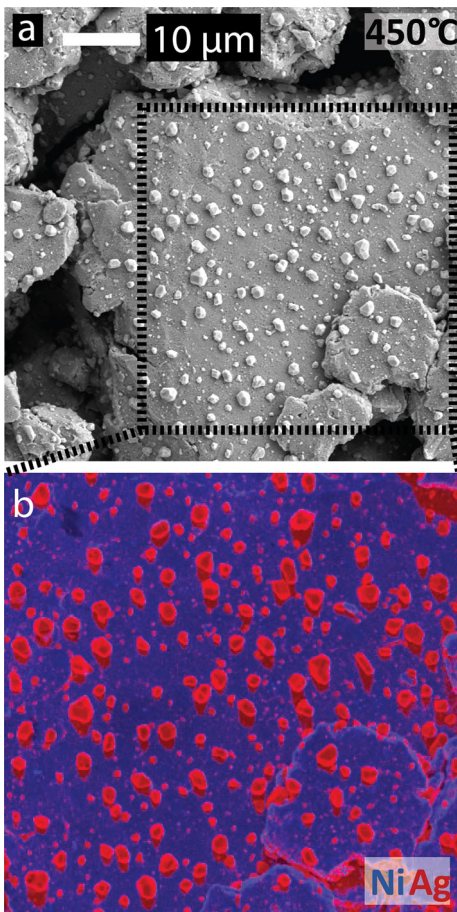

Fig. 4—Scanning electron microscopy (SEM) images of the ball-milled Ni–Ag powders annealed at 450 °C (a). The chemical mapping (EDS) is done on the highlighted region (b) indicating that the precipitates on the Ni powder surface are Ag-rich.

IV. SINTERING

For the sintering experiments, the ball-milled Ni–Ag powders are cold-compacted into cylinders with a typical height and diameter of ~ 2 and 6 mm, respectively, using a uniaxial hydraulic press (YLJ-15L from MTI Corporation) and a pressure of 400 to 450 MPa acting on the pellets. The initial relative density is in the range of 56 to 59 pct, calculated from the ratio of initial and theoretical density (9.2 g/cm^3, from the atomic weight). In the following, we present the sintering behavior of the Ni–Ag powders and quantify the evolution of microstructure and relative density upon heating. This is complemented by an analysis of the gas evolution and nano-phase separation kinetics.

Since we expect the microstructure to evolve on several length scales—on the macroscale with an overall reduction of porosity in the green compact facilitated by the nano-phase separation of an interparticle Ag phase on (initially) a 1 to 10 μm scale, we track the changes of the relative density in the compacts at different sintering temperatures by inspecting micrographs at different magnifications. The Ni–Ag compacts are heated at a rate of 5 °C/min to various final temperatures (450 °C, 550 °C, 650 °C, 700 °C, 790 °C, 800 °C, 810 °C and 830 °C) in a protective atmosphere of Ar containing 4 pct H_2, and subsequently rapidly cooled at a rate of 40 °C/min. Samples heated to temperatures above 700 °C are water-quenched to prevent the microstructure from evolving upon cooling. To characterize the microstructure, samples are cold-mounted, mechanically ground and polished in a standard preparation routine and imaged on a ZEISS Gemini 450 scanning electron microscope (SEM) at secondary electron mode. Porosity of the microstructures is based on the assessment of 3 to 5 microstructural images of the same sample and quantified using ImageJ software.

Figure 5 compiles a set of micrographs showing the compact structure at various scales and different temperatures. The images are presented in such a way as to facilitate comparison across length scales; for each subfigure label (e.g., Figure 5(a)) there are three images (a1, a2, and a3) in which the structure is shown at the same magnification with the same scale bar. The upper and middle blocks of microstructures display the evolution on a larger scale ($\gg 1$ μm), while those in the lower block are higher magnification images focused on the submicron structure.

Looking first at the coarser length scales in Figure 5, the microstructures suggest a sequence that is expected for a sintering process—a gradual densification up to 650 °C, with a clear acceleration of consolidation between 700 °C and 790 °C to a relatively high density where some pores have become isolated. However, at higher temperatures this trend is followed by a reversal—a decreasing relative density as the powders apparently detach from each other and the porosity reopens into more of a network. Upon closer inspection, this swelling or foaming process is heralded already by micrographs at a finer scale (bottom block of microstructures in Figure 5): small nano-scale porosity emerges inside the powders above about 450 °C and
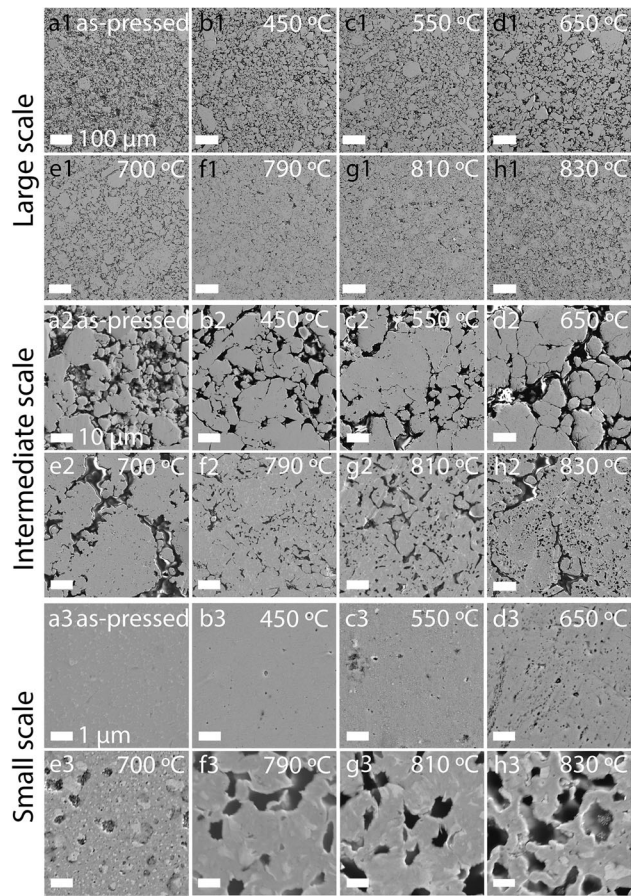
Fig. 5—Microstructural evolution of the Ni–Ag powder compacted (*a*) and sintered to different temperatures (*b*) through (*h*). Each sample is denoted by a specific letter and shown at three different magnifications (1 to 3) to capture microstructural features, such as pores, between and inside of powder particles on all length scales. The scale bars for each scale (large, intermediate, and small) are the same as for the labelled length. The interparticle and intraparticle porosity in the Ni–Ag sample are apparently decoupled, with a clear emergence and growth of the latter to a considerable area fraction upon sintering to higher temperatures.

expands to cover a substantial fraction of the intra-particle area.

While the foaming seen in Figure 5 is not desirable in a sintering process, it is in line with our prior work on fast-sintering nanocrystalline Ni powder compacts,[47] and reflects the evolution of gas that does not occur early enough to escape the compact. The changes in pore morphology seen here are also in line with that prior work. Figure 6 reviews the evolution of the average pore size (a) and aspect ratio (b) obtained from the image analysis of the micrographs above. The full distributions of both characteristics are given in the supplemental material (Fig. S2). The trends are investigated for the inter-particle (top set of microstructures in Figure 5) and intra-particle porosity (bottom set). Whereas the porosity between the powder particles gradually changes shape and suggests densification on a larger scale (as we expect by alloying of a sintering accelerant), the fine pores inside the powders stretch considerably, reaching a maximum aspect ratio at 800 °C. In contrast, the intraparticle pores remain well

below sub-micron in size until they increase by about one order of magnitude above the same temperature. With such scale-dependent microstructural behavior, we define two measurable porosity fractions, p_{inter} and p_{intra} to refer to the corresponding porosities in the inter- and intra-particle regions of the sintered compacts, respectively. The evolution of p_{inter} and p_{intra} is displayed in Figure 7(a) and confirms the densification on a large scale (by reduction of the porosity by half as compared to the initial green compact), whereas a significant build-up of porosity inside the powder takes place (~ 44 pct) at 830 °C.

To compare the porosity extracted from the micrographs with volumetric shape changes upon sintering, some Ni–Ag powder compacts are subjected to thermo-mechanical analysis on a TMA 402 F3 Hyperion from NETZSCH in a protective Ar atmosphere with 4 pct forming gas (H_2). Various heating rates between 3 °C/min and 50 °C/min are applied up to a final sintering temperature of 945 °C, followed by an immediate cooling at a rate of 40 °C/min. The change in raw length of the powder pellets is converted into densification by assuming isotropic volumetric shrinkage behavior of the powder, which agrees generally (within about 5 pct margin) with caliper measurements post-sintering.

Figure 7(b) shows the change in relative density of the sintered Ni–Ag pellets, including an initial phase of densification and then a protracted swelling, with an overall loss in relative density after the thermal cycle. To align the results of the microstructure analysis with the dilatometric measurements, a general composite porosity can be determined by

$$P_{total} = P_{inter} + (1 - P_{inter})P_{intra} \qquad [3]$$

which accounts for the fact that when measuring the coarse-scale interparticle porosity, the finer scale porosity is not observable (cf. Figure 5); the total porosity is the sum of the two components and the intraparticle component is only measured within the area of the particles $(1 - p_{inter})$. Such stereological measurements of porosity are shown as a series of data points (black markers) in Figure 7(b) and are in overall good agreement with the dilatometry analysis.

Both change in shape and microstructure suggest a foaming process, i.e., loss in relative density, by a sequence of two events (~ 450 °C and 800 °C). To complement volume and weight evolution of the samples, the change in relative weight is shown in Figure 7(c), indicating a loss of about 0.6 pct as compared to the initial compact weight. The major contribution of the mass change takes place at temperatures above 600 °C.

The foaming process is driven by gas evolution, which, as laid out in Reference 47, is associated with organic burn-off as well as reduction of native oxides by the carbon from the organics of the ball-milled powders. To observe the gas evolution of the system, mass spectrometer measurements are performed on a QMS 403 Aeolos from NETZSCH, using cylindrical Ni–Ag pellets with extended dimensions of ~ 10 and 2 mm for diameter and height, respectively, and increased weight
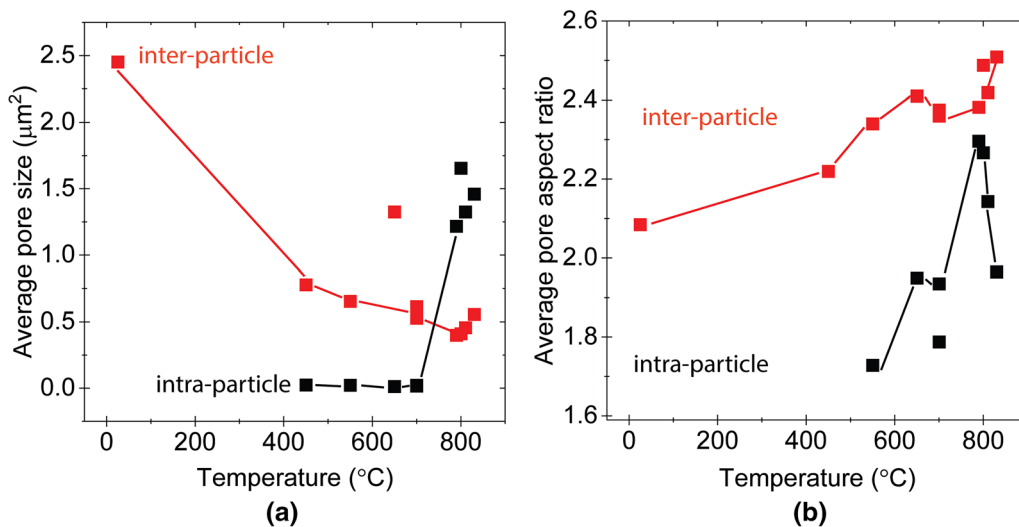
Fig. 6—Quantitative evolution of pore characteristics, i.e., size (*a*) and aspect ratio (*b*), during sintering, individually considered for inter- and intraparticle porosity (red and black markers, respectively). As expected for a sintering process, the red line in (a) shows rapid pore size decrease upon heating, but this is complicated by the development of intra-particle porosity (black line). The pores elongate (b) due to creep growth and coalescence characteristic of creep foaming of the powder compact (Color figure online).

of 0.8 g to amplify the signals characteristic for the gas species. The powder compacts are pressed and heated up to 940 °C at a rate of 10 °C/min and subsequently cooled at 40 °C/min under a high purity Ar atmosphere such that all other gases measured by the spectrometer are evolution products from the sample.

To clearly reveal the quantitative relation between gas evolution, mass loss and foaming in Ni–Ag, Figure 8 shows the time-derivatives of densification (a) and mass change (b) over the sintering range in addition to the detected volatile gaseous species as obtained from the mass spectrometer analysis (c). As heating begins, at a very low-temperature of about 100 °C, we observe the loss of hydrogen and water from the sample at the same point where we detect some mass loss, but at this point there is not yet any suggestion of either sintering or swelling; the powder compact is probably unchanged from its as-pressed condition, and easily releases these gases through the open porosity network. At higher temperatures, however, there are two apparent swelling peaks in the densification behavior of the pellets, one minor one at ~ 450 °C and a major one between 800 °C and 900 °C. To guide the attention of the readers through the remainder of this paper, we reference to these two swelling peaks by labels (i) and (ii) (cf. Figure 8).

Swelling event (i) occurs at the lower temperature of 450 °C, and is not associated with any major release of gas as can be seen in Figures 8(b) and (c). On the contrary, the mass loss rate closely approaches zero at ~ 430 °C right before the first swelling peak. The slight uptick in CO around this temperature suggests a mechanism for this swelling event: the sudden development of CO gas internally in the sample, which is largely trapped and becomes a foaming agent from this point forward. By contrast, the second main swelling event (ii) is clearly accompanied by a distinct change in relative weight, and by substantial release of CO and CO_2.

It is known that powders release fugitive species from their surface during annealing,[69–71] and such off-gassing is expected and planned for green bodies formed with additions of organic additives, such as in binder jetting[72] or bound metal deposition operations.[38] In the case of ball-milled powders, the process control agent (in the present case ethanol, C_2H_6O) is the main source of hydrogen, carbon, and oxygen, and the gas evolution is largely linked with its recombination. This is complicated by the available C causing the reduction of native oxides,[71,73] which initiates a release of gas that is known to cause swelling in nanocrystalline metals.[47] This is very typical for elements that exhibit a high tendency for oxide reduction.[71,73] Particularly for Ni, the thermodynamic instability of NiO in the presence of C facilitates the redox reduction:

$$2\,NiO + C \rightarrow Ni + CO_2 \qquad [4]$$

which has an activation energy of ~ 87 kJ/mol with formation enthalpies for ΔH_{CO_2} (− 393 kJ/mol[66,74]) and ΔH_{NiO} (− 240 kJ/mol[67,75]), as well as entropies for ΔS_{CO_2} (213.8 J/Kmol[76]), ΔS_{NiO} (38.1 J/Kmol), ΔS_{Ni} (29.9 J/Kmol) and ΔS_C (5.7 J/Kmol). However, the classical Ellingham-Richardson diagram suggests a thermodynamic equilibrium temperature of ~ 220 °C for the chemical reaction in Eq. [4] (which is likely to occur rather than the formation of less stable CO).[71,73] This is below the point where we first observe a significant swelling signal and a release of CO at ~ 430 °C, and far below the temperature observed for the release of C-based gaseous species (see Figure 8(c)) at 800 °C, which is untypically high for burn-off of organic additives typically observed in many additive manufacturing technologies, such as binder jetting of Inconel.[44,45] This is particularly interesting as the process organics only make up 5 pct of the weight of the powder in this work, which is a much smaller volume fraction than in binder jetting approaches; our results
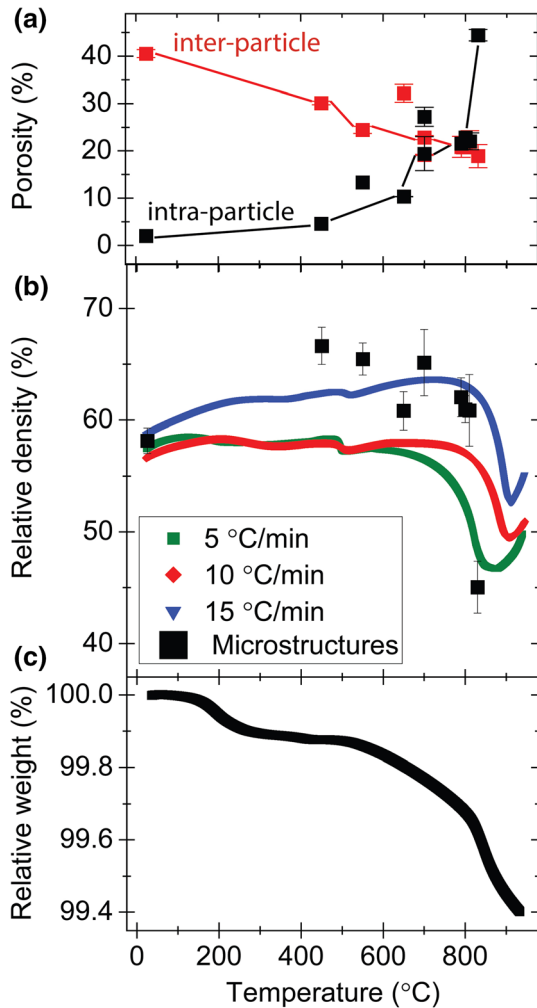
Fig. 7—(a) Evolution of inter- and intraparticle porosity in the Ni–Ag powder upon sintering, as extracted from the micrographs in Fig. 5. Whereas the porosity at the large scale (from the compacted green body) gradually vanishes, porosity emerges within the powder particles. (b) Relative density of the sintered Ni–Ag powder, as obtained from dilatometry measurements for different heating rates and calculated from the inter- and intraparticle porosity. Instead of undergoing densification, the powder compacts exhibit swelling behavior with a significant loss of relative density at the end of the heating cycle. At the same time, the samples apparently lose some mass (c).

thus project even more severe microstructural evolution in a 3D printing context, i.e., the present work presents something of a lower bound to the problem. We focus on the gas evolution and the microstructural swelling based on thermodynamic and kinetic aspects next.

V. KINETICS OF GAS EVOLUTION AND MICROSTRUCTURAL SWELLING

A. Initial Swelling (i)

The minor first swelling event in Figures 7 and 8 is characterized by the initial formation of fine-scaling intra-particle porosity (see micrographs at the fine scale in Figure 5), leading to a small degree of swelling
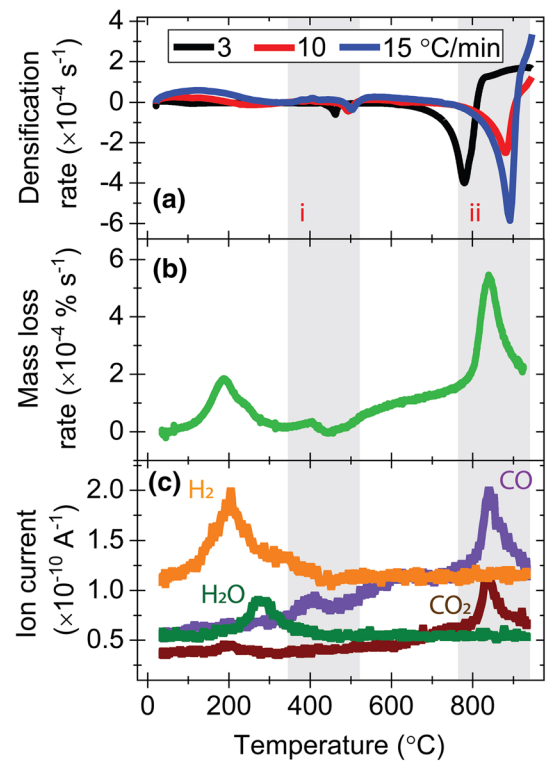

Fig. 8—The derivative of the raw dilatometry data (a) suggests a series of two swelling events at 450 °C and 900 °C with appropriate temperature ranges labelled as i and ii. As compared to the derivative of the raw mass evolution, two peaks emerge as H_2- and C-based gaseous species evolve (b, c). Whereas the former is not accompanied with swelling, the onset temperature of the second falls at a temperature above the point where phase separation occurred, trapping the gas and leading to excessive sample expansion.

(Figure 7(b)) without any noticeable change in compact weight (Figure 8(b)). The equilibrium temperature for the chemical reaction [4] is almost 200 °C lower than for the first swelling in the sintered Ni–Ag pellet. This thermal lag has been seen before in our prior work on sintering of nanocrystalline Ni,[47] and was attributed to the slow kinetics of carbon diffusion out of the bulk, where it resides after milling. To assess the rate-limitation mechanism for the initial swelling (i), we employ a Kissinger-style kinetic analysis based on diffusional processes.[77] Figure 9(a) exhibits this analysis using the swelling peaks for various heating rates q (in Figure 8(a)). Faster heating rates will slightly delay the process and therefore shift the onset to higher temperatures with q/T in an Arrhenius-type manner. Thus, the slope in Figure 9(a) is $-Q/R$, which by fitting the data yields an activation energy of ~ 120 kJ/mol. This value is noticeably higher than the energy required for the chemical reaction (~ 87 kJ/mol for Eq. [4]), but is very close to the bulk diffusion of C in Ni at 137 kJ/mol.[78] This analysis conforms with that in nanocrystalline Ni quite exactly; the first evolution of gas is rate-limited by carbon diffusing out of the grains. Readers are referred to that work for deeper discussion of the mechanistic details.[47]
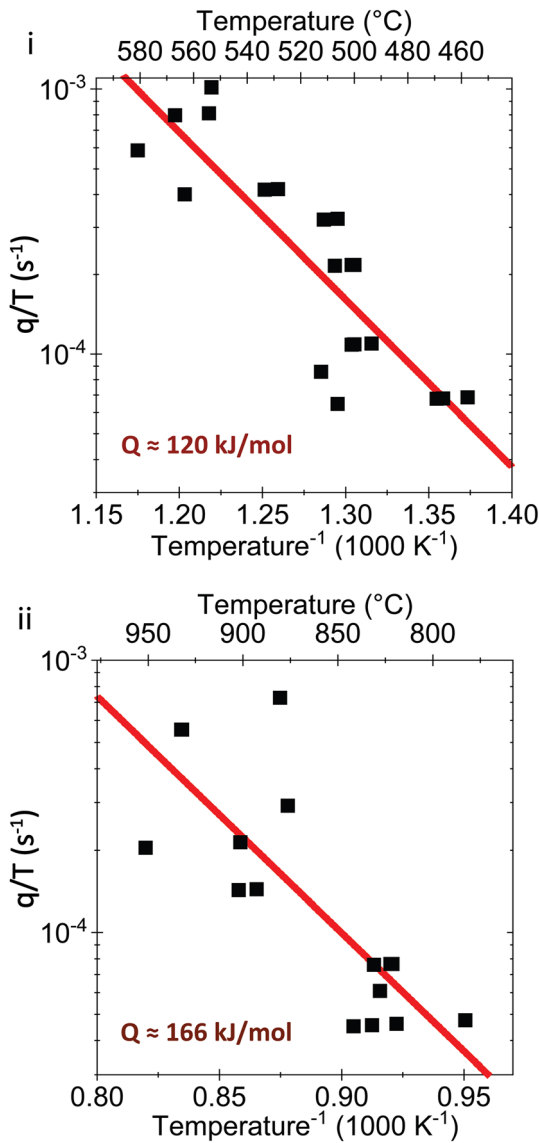
Fig. 9—Kissinger-style kinetic analysis for the case of diffusion rate-limitation on the swelling events (i and ii) in the densification rate curves in Fig. 7(a). From the slopes, energies of 120 and 166 kJ/mol are extracted, which are good fits to the activation energies of bulk diffusion of C in Ni and self-diffusion of Ag.

B. Major Release of Volatilizing Gas (ii)

The main loss in relative density in this system takes place above 800 °C, which is preceded by a maximum in mass release (cf. Figures 8(a) and (b)) and a drastic change in the microstructure on all length scales (cf. Figure 5): whereas large interparticle porosity gradually vanishes between the powder particles as 800 °C is approached, this is followed by new emerging gaps between neighboring particles for higher temperatures, as well as fine spherical pores steadily growing inside the powders. Eventually these tremendously expand in size and aspect ratio at the end of the sintering cycle. In our prior studies on nanocrystalline Ni, we proposed that gas evolved at the first swelling peak can remain trapped

and pressurize upon heating, leading to creep-swelling of the structure at higher temperatures. Particularly the pore shape evolution is a clear indicator for creep swelling: at the early stages the adoption of a rather spherical shape of the intra-particle porosity is suggestive of trapped gas, while at temperatures of 800 °C and above, previously isolated pores become more interconnected and form a network of high aspect-ratio pores; cell wells burst and gas is again able to escape the open porosity network.

Another point supporting this interpretation is the kinetic rate-limitation for the swelling process, which we can treat with the same Kissinger-style kinetic analysis used above,[77] as shown in Figure 9(b). The slope of the rate-peak analysis gives an activation energy of 166 kJ/mol, which is very close to expectations for rate limitation by creep of the silver phase (165 to 185 kJ/mol),[79] and very far from the activation energy for creep of Ni observed in our prior work without silver (∼ 300 kJ/mol).[47] In that prior work, we noted that creep of Ni was a possible rate-limiting mechanism, but due to the similarity of the activation energy with other processes this conclusion was tentative. In the present case of a two-phase material the creep of the faster phase should limit the kinetics,[80] so the present observation is significant: the addition of fast-creeping silver lowers the activation energy as expected for a creep mechanism (see Fig. S6). The present experiments thus provide more conclusive evidence that indeed, swelling is creep limited in these systems.

These results thus speak to new design considerations for phase-separating sintering systems, and call for alloy selection efforts that specifically aim to separate gas evolution from phase separation. Not only can the phase separation event facilitate the trapping of gases internally, it can also provide fast-creeping phases that accelerate the swelling once gas is present. In prior work[47] it has been suggested that powder pre-treatments or the inclusion of gettering elements may be needed to offset the gas evolution problem in nanocrystalline materials generally, and such approaches may be needed in phase-separating systems as well based on the present results.

VI. CONCLUSION

The objective of this work was to design a Ni–Ag powder compact that was mechanically alloyed to a condition ripe for phase separation, which in turn affects the sintering process of the powder upon heating. In line with theory for driven systems, the Ni–Ag system can be made to dissolve just about 12 at. pct Ag, leading to a significant driving force for decomposition upon heating. The powders showed that phase separation at a temperature of only ∼400 °C through an out-of-equilibrium state of the powders driven by both a nanocrystalline structure and solute concentration far beyond the solubility limit. However, this phase separation also leads to low-temperature sintering processes taking place. The second phase formed preferentially on free surfaces, i.e., interparticle necks and also free pore surfaces, and as a result gas evolving from the dissolving

organic processing aids (which were added to enable the initial ball milling process), was trapped and formed pores inside the powders. The net result is delayed organic burn-off and enhanced kinetics of creep foaming in the powder compact.

The interplay between densification and oxide removal was recently investigated for nanocrystalline metal powders but has been extended in this work also to alloy powders that were designed to accelerate sintering, and is relevant to synthesis strategies that aim to increase the rate of pressure-free solid-state sintering. In order to avoid the described competition between densification and organic debinding from the powder, one might contemplate pre-treatment for the complete removal of organic residuals prior to the onset of consolidation, whereas the sintering temperatures can be roughly estimated for each element depending on its melting temperature and structure.[47] There are particular elements (see Reference 47) that enable low-temperature sintering, such as in a nanocrystalline structure, either by oxide reduction (and degassing) before the onset of sintering (e.g., W) or by providing a stable oxide compound throughout the entire sintering cycle (e.g., Al). The latter approach suggests that components of the added organics are locked down rather than volatilize completely as typical in standard debinding routines in additive manufacturing. We are not aware that these approaches have been documented for phase-separating sintering situations in prior work, but the present results suggest they will be explored in the future.

ACKNOWLEDGMENTS

FUNDING

CONFLICT OF INTEREST

MIT has filed patents on nanophase separation sintering, including on some of the concepts present in this work. On behalf of all authors, the corresponding author states that there is no conflict of interest.

OPEN ACCESS

SUPPLEMENTARY INFORMATION

The online version contains supplementary material available at https://doi.org/10.1007/s11661-023-07152-3.

REFERENCES

1. M. Molitch-Hou: in *Additive Manufacturing*, Elsevier, Amsterdam, 2018, pp. 1–38.
2. T. DebRoy, H.L. Wei, J.S. Zuback, T. Mukherjee, J.W. Elmer, J.O. Milewski, A.M. Beese, A. Wilson-Heid, A. De, and W. Zhang: *Prog. Mater. Sci.*, 2018, vol. 92, pp. 112–24.
3. M.K. Thompson, G. Moroni, T. Vaneker, G. Fadel, R.I. Campbell, I. Gibson, A. Bernard, J. Schulz, P. Graf, B. Ahuja, and F. Martina: *CIRP Ann. Manuf. Technol.*, 2016, vol. 65, pp. 737–60.
4. W.J. Sames, F.A. List, S. Pannala, R.R. Dehoff, and S.S. Babu: *Int. Mater. Rev.*, 2016, vol. 61, pp. 315–60.
5. A. Bose, C.A. Schuh, J.C. Tobia, N. Tuncer, N.M. Mykulowycz, A. Preston, A.C. Barbati, B. Kernan, M.A. Gibson, D. Krause, T. Brzezinski, J. Schroers, R. Fulop, J.S. Myerberg, M. Sowerbutts, Y.M. Chiang, A. John Hart, E.M. Sachs, E.E. Lomeli, and A.C. Lund: *Int. J. Refract. Met. Hard Mater.*, 2018, vol. 73, pp. 22–8.
6. S.M. Allen and E.M. Sachs: *Met. Mater. Int.*, 2000, vol. 6, pp. 589–94.
7. M. Ziaee and N.B. Crane: *Addit. Manuf.*, 2019, vol. 28, pp. 781–801.
8. D.D. Gu, W. Meiners, K. Wissenbach, and R. Poprawe: *Int. Mater. Rev.*, 2012, vol. 57, pp. 133–64.
9. W.J. Huppmann and H. Riegger: *Acta Metall.*, 1975, vol. 23, pp. 965–71.
10. R.M. German, P. Suri, and S.J. Park: *J. Mater. Sci.*, 2009, vol. 44, pp. 1–39.
11. P. Lee, H. Chung, S.W. Lee, J. Yoo, and J. Ko: in *Materials; Micro and Nano Technologies; Properties, Applications and Systems; Sustainable Manufacturing*, vol. 1, American Society of Mechanical Engineers, New York, 2014, pp. 1–8.
12. B.N. Turner and S.A. Gold: *Rapid Prototyp. J.*, 2015, vol. 21, pp. 250–61.
13. E.R. Denlinger, J.C. Heigel, P. Michaleris, and T.A. Palmer: *J. Mater. Process. Technol.*, 2015, vol. 215, pp. 123–31.
14. A.S. Wu, D.W. Brown, M. Kumar, G.F. Gallegos, and W.E. King: *Metall. Mater. Trans. A Phys. Metall. Mater. Sci.*, 2014, vol. 45, pp. 6260–70.

15. S.A. Khairallah, A.T. Anderson, A. Rubenchik, and W.E. King: *Acta Mater.*, 2016, vol. 108, pp. 36–45.
16. M. Grasso and B.M. Colosimo: *Meas. Sci. Technol.*, 2017, https://doi.org/10.1088/1361-6501/aa5c4f.
17. H.L. Wei, J. Mazumder, and T. DebRoy: *Sci. Rep.*, 2015, vol. 5, pp. 1–7.
18. F. Zhang, L.E. Levine, A.J. Allen, M.R. Stoudt, G. Lindwall, E.A. Lass, M.E. Williams, Y. Idell, and C.E. Campbell: *Acta Mater.*, 2018, vol. 152, pp. 200–14.
19. D.N. Yoon and W.J. Huppmann: *Acta Metall.*, 1979, vol. 27, pp. 693–98.
20. I.J. Toth and N.A. Lockington: *J. Less Common Met.*, 1967, vol. 12, pp. 353–65.
21. G.V. Samsonov and V.I. Yakovlev: *Soviet Powder Metall. Met. Ceram.*, 1969, vol. 8, pp. 804–08.
22. H.W. Hayden and J.H. Brophy: *J. Electrochem. Soc.*, 1963, vol. 110, p. 805.
23. V.V. Panichkina, V.V. Skorokhod, and A.F. Khrienko: *Soviet Powder Metall. Met. Ceram.*, 1967, vol. 6, pp. 558–60.
24. H.J. Ryu, S.H. Hong, and W.H. Baek: *Mater. Sci. Eng. A*, 2000, vol. 291, pp. 91–96.
25. J.L. Johnson and R.M. German: *Metall. Mater. Trans. A Phys. Metall. Mater. Sci.*, 1996, vol. 27, pp. 441–50.
26. R.M. German and Z.A. Munir: *Metall. Trans. A*, 1976, vol. 7, pp. 1873–77.
27. M.T. Stawovy, K. Myers, and S. Ohm: *Int. J. Refract. Met. Hard Mater.*, 2019, vol. 83, 104981.
28. R.K. Enneti, K.C. Prough, T.A. Wolfe, A. Klein, N. Studley, and J.L. Trasorras: *Int. J. Refract. Met. Hard Mater.*, 2018, vol. 71, pp. 28–35.
29. R.K. Enneti and K.C. Prough: *Int. J. Refract. Met. Hard Mater.*, 2019, vol. 78, pp. 228–32.
30. M. Park and C.A. Schuh: *Nat. Commun.*, 2015, vol. 6, p. 6858.
31. T. Chookajorn, M. Park, and C.A. Schuh: *J. Mater. Res.*, 2015, vol. 30, pp. 151–63.
32. M. Park, T. Chookajorn, and C.A. Schuh: *Acta Mater.*, 2018, vol. 145, pp. 123–33.
33. N.C. Kothari: *J. Less Common Met.*, 1967, vol. 13, pp. 457–68.
34. R.M. German: *Metall. Mater. Trans. A.*, 1995, vol. 26A, pp. 279–88.
35. S.-M. Lee and S.-J.L. Kang: *Acta Mater.*, 1998, vol. 46, pp. 3191–202.
36. J. Luo, V.K. Gupta, D.H. Yoon, and H.M. Meyer: *Appl. Phys. Lett.*, 2005, vol. 87, 231902.
37. V.K. Gupta, D.-H. Yoon, H.M. Meyer, and J. Luo: *Acta Mater.*, 2007, vol. 55, pp. 3131–42.
38. A. Bose, A.C. Lund, J.P. Reidy, C.A. Craven, M.A. Gibson, A.C. Barbati, C.A. Schuh, L. Jorgensen, J.C. Tobia, A. Dias, and N. Tuncer: *Int. J. Powder Metall.*, 2021, vol. 57, pp. 17–30.
39. Y. Bai and C.B. Williams: *Rapid Prototyp. J.*, 2015, vol. 21, pp. 177–85.
40. B. Verlee, T. Dormal, and J. Lecomte-Beckers: *Powder Metall.*, 2012, vol. 55, pp. 260–67.
41. M. Ziaee, E.M. Tridas, and N.B. Crane: *JOM*, 2017, vol. 69, pp. 592–96.
42. A.K. Dhaliwal and J.N. Hay: *Thermochim. Acta*, 2002, vol. 391, pp. 245–55.
43. M.A. Moharram and M.G. Khafagi: *J. Appl. Polym. Sci.*, 2006, vol. 102, pp. 4049–57.
44. P. Nandwana, A.M. Elliott, D. Siddel, A. Merriman, W.H. Peter, and S.S. Babu: *Curr. Opin. Solid State Mater. Sci.*, 2017, vol. 21, pp. 207–18.
45. A. Mostafaei, J. Toman, E.L. Stevens, E.T. Hughes, Y.L. Krimer, and M. Chmielus: *Acta Mater.*, 2017, vol. 124, pp. 280–89.
46. E. Hnatkova, B. Hausnerova, A. Hales, L. Jiranek, F. Derguti, and I. Todd: *Powder Technol.*, 2017, vol. 322, pp. 439–46.
47. Y. Naunheim and C.A. Schuh: *Acta Mater.*, 2023, vol. 247, 118743.
48. H. Massalski, R.P. Okamoto, L. Subramanian, and T.B. Kacprzak: *Binary Alloy Phase Diagrams*, 2nd ed. ASM International, Metals Park, 1990.
49. M. Singleton and P. Nash: *J. Phase Equilib.*, 1987, vol. 8, pp. 119–21.
50. H. Okamoto: *J. Phase Equilib. Diffus.*, 2013, vol. 34, pp. 493–505.
51. G. Cocco, S. Enzo, N.T. Barrett, and K.J. Roberts: *Phys. Rev. B*, 1992, vol. 45, p. 7066.
52. A.O. Aning, I.Z. Wang, and T.H. Courtney: *Acta Metall. Mater.*, 1993, vol. 41, pp. 165–74.
53. Y. Ashkenazy, N.Q. Vo, D. Schwen, R.S. Averback, and P. Bellon: *Acta Mater.*, 2012, vol. 60, pp. 984–93.
54. J. Xu, U. Herr, T. Klassen, and R.S. Averback: *J. Appl. Phys.*, 1996, vol. 79, pp. 3935–945.
55. Z.C. Cordero and C.A. Schuh: *Acta Mater.*, 2015, vol. 82, pp. 123–36.
56. Z.C. Cordero, B.E. Knight, and C.A. Schuh: *Int. Mater. Rev.*, 2016, vol. 6608, pp. 1–8.
57. E.E. Underwood: *Quantitative Stereology*, Addison-Wesley, Reading, 1970.
58. G.K. Williamson and W.H. Hall: *Acta Metall.*, 1953, vol. 1, pp. 22–31.
59. C. Suryanarayana: *Prog. Mater. Sci.*, 2001, vol. 46, pp. 1–84.
60. L. Vegard: *Z. Phys.*, 1921, vol. 5, pp. 17–26.
61. D. Bonyuet, J. Ochoa, and G. González: *J. Metastable Nanocryst. Mater.*, 2004, vol. 20–21, pp. 225–30.
62. Z.L. Zhao, Y. Niu, F. Gesmundo, and C.L. Wang: *Oxid. Met.*, 2000, vol. 54, pp. 559–74.
63. A. Bachmaier, J. Keckes, K.S. Kormout, and R. Pippan: *Philos. Magn. Lett.*, 2014, vol. 94, pp. 9–17.
64. D. Amram and C.A. Schuh: *Scr. Mater.*, 2020, vol. 180, pp. 57–61.
65. F. Delogu and G. Cocco: *Mater. Sci. Eng. A*, 2006, vol. 422, pp. 198–204.
66. C.W. Sinclair, J.D. Embury, and G.C. Weatherly: *Mater. Sci. Eng. A*, 1999, vol. 272, pp. 90–98.
67. G. Reglitz, B. Oberdorfer, N. Fleischmann, J.A. Kotzurek, S.V. Divinski, W. Sprengel, G. Wilde, and R. Würschum: *Acta Mater.*, 2016, vol. 103, pp. 396–406.
68. T.J. Rupert, J.R. Trelewicz, and C.A. Schuh: *J. Mater. Res.*, 2012, vol. 27, pp. 1285–94.
69. Y. Sakka and T. Uchikoshi: *Powder Metall.*, 1993, vol. 36, pp. 179–85.
70. Y. Sakka, T. Uchikoshi, E. Ozawa, and E. Ozawa: *Mater. Trans. JIM*, 1990, vol. 31, pp. 802–09.
71. H.J.T. Ellingham: *J. Soc. Chem. Ind.*, 1944, vol. 63, pp. 125–33.
72. R. Jiang, L. Monteil, K. Kimes, A. Mostafaei, and M. Chmielus: *Int. J. Adv. Manuf. Technol.*, 2021, vol. 116, pp. 3827–38.
73. F.D. Richardson: *J. Iron Steel Inst.*, 1953, vol. 175, pp. 33–51.
74. B. Ruscic, D. Feller, and K.A. Peterson: *Theor. Chem. Acc.*, 2014, vol. 133, pp. 1–2.
75. R.D. Holmes, H.S.C. O'Neill, and R.J. Arculus: *Geochim. Cosmochim. Acta*, 1986, vol. 50, pp. 2439–52.
76. M.W. Chase, Jr.: in *Journal of Physical and Chemical Reference Data Monograph*, vol. 9, 4th ed., American Chemical Society, 1998, pp. 1–1951.
77. C. Oliver and C.A. Schuh: *Metall. Mater. Trans. A Phys. Metall. Mater. Sci.*, 2021, vol. 52, pp. 4479–87.
78. W.F. Gale and T.C. Totemeier: *Smithells Metals Reference Book*, Elsevier, 2003.
79. M.F. Ashby: *Acta Metall.*, 1974, vol. 22, pp. 275–89.
80. I.W. Chen: *Acta Metall.*, 1982, vol. 30, pp. 1655–64.